ROYAL SOCIETY OPEN SCIENCE

royalsocietypublishing.org/journal/rsos

Research

Cite this article: Allgood C, Jones TJ. 2026 Breakup dynamics of Newtonian fluids under extension. *R. Soc. Open Sci.* **13**: 252527.
https://doi.org/10.1098/rsos.252527

Received: 23 December 2025
Accepted: 13 January 2026

Subject Category:
Physics and biophysics

Subject Areas:
mathematical physics, volcanology, fluid mechanics

Keywords:
fluid dynamics, fluid breakup dynamics, fluid filaments, extensional flow, capillary thinning rheometry, filament stretching rheometry, volcanology

Author for correspondence:
Ceri Allgood
e-mail: c.allgood1@lancaster.ac.uk

Supplementary material is available online at https://doi.org/10.6084/m9.figshare.c.8285021.

THE ROYAL SOCIETY PUBLISHING

Breakup dynamics of Newtonian fluids under extension

Ceri Allgood and Thomas J. Jones

Lancaster Environment Centre, Lancaster University, Lancaster, UK

CA, 0009-0007-7878-1811; TJJ, 0000-0003-4981-5131

When a Newtonian fluid is stretched via uniaxial extension, it forms a narrow filament which thins until it breaks. Thinning is governed by mechanical forces, whereby an increase in filament length necessitates a reduction in width, and by capillary forces, whereby the rate of capillary thinning depends on the fluid's viscosity and surface tension. The timing of filament breakup is a key parameter in understanding fluid fragmentation, droplet formation and the maximum filament length achievable, which are relevant to many natural and industrial processes, from volcanic eruptions to spray paints. Here, we perform uniaxial extension experiments on Newtonian silicone oils stretched between circular, parallel plates moving at equal and opposite velocities. We find that filament breakup always occurs in a regime dominated by capillary forces, irrespective of the plate separation rate, and that breakup time can be reliably predicted from initial fluid dimensions, plate separation rate and the ratio of surface tension to viscosity. As an illustration of use, we apply our findings to an example of a volcanic eruption, predicting the maximum length of fluid filaments that could be produced by clasts of ejected lava breaking up mid-flight.

1. Introduction

Extensional flows occur in a range of settings. Industrial and manufacturing processes produce extensional flows under a range of conditions, from high-energy fluid jets to low-energy falling droplets, with examples including three-dimensional printing and filling containers. In many cases, fluids break up under extensional conditions, generating sprays or droplets, with examples including fire suppression systems, paint coating, metal powder production and agricultural pesticide treatments [1]. There are also a range of natural processes in which fluid extension and associated breakup play a crucial role, such as the

generation of sea spray and marine droplets [2], the cascading breakup of rain droplets governing their final size distribution [3], the properties of biological silks such as spider's webs [4] and the extension and fragmentation of high-temperature silicate melts during volcanic eruptions [5,6].

The breakup of fluid jets into droplets has been studied extensively [7–9], with applications to taps, hoses and nozzles. However, the breakup of fluids that are stretched into filaments is less well-studied, despite this process being relevant to many industrial and natural processes. The maximum thread length that can be produced by stretching a fluid at a specified rate influences the size distribution of droplets once the thread eventually breaks, with implications for spray formation. In cases where the fluid is drying, curing or solidifying as it is being stretched, the maximum thread length determines the shape of the resulting solid structure; for example, the stretching of magma in volcanic eruptions is known to produce micrometre-scale glassy filaments known as 'Pele's hair' under certain conditions [10,11]. The maximum thread length, which can be pitched, equivalently, as a filament breakup time, is therefore a crucial parameter for understanding the dynamics of extensional fluid breakup.

Many methods have been developed to investigate the extensional properties of fluids. The most used methods involve stretching fluids into filaments to determine their extensional viscosities and viscoelastic properties, typically by trapping a fluid between two parallel, circular plates, then moving these plates apart. Filament stretching extensional rheometry (FiSER) involves separating the plates at a specified, increasing rate in order to impose a constant extensional strain rate at the fluid filament mid-plane, then measuring the resulting force on one of the plates (e.g. [12,13]). Capillary breakup extensional rheometry involves suddenly separating the plates to a specified distance, essentially applying a step strain to the fluid, before allowing the filament to thin via internal capillary forces, and monitoring its change in diameter (e.g. [14,15]). Neither of these methods is designed with the primary aim of investigating breakup; instead, they focus on the fluid properties governing thinning. For this reason, we refer to capillary breakup experiments as capillary thinning experiments to avoid confusion [15]. We note that there are other variations of capillary thinning experiments, such as dripping-on-substrate [16–18] and the slow retraction method [19,20], but the fundamentals of these methods are the same.

Neither FiSER nor capillary thinning experiments capture the conditions present in the natural environment or in industrial settings, where filament stretching is likely to occur at either a constant or variable rate, rather than being exponential or instantaneous. The two types of extensional rheometry define opposite ends of a behavioural spectrum: FiSER experiments force the fluid to experience a specified strain rate owing to applied mechanical stretching, whereas capillary thinning experiments allow the fluid to select its own thinning time scale, driven by internal capillary forces. Most natural or industrial examples of fluid stretching will fall somewhere between these end-member scenarios: the fluid will experience some amount of mechanical stretching, but it will also thin under capillary forces at the same time.

Here, we present experiments that fall between these end-member scenarios, exploring the conditions in which fluids thin under combined mechanical and capillary forces. Our experiments involve small volumes of Newtonian fluid being stretched between circular endplates moving apart at constant and opposite velocities. We use high-speed videography to capture the evolution of the stretching fluid thread, to establish the nature of the dynamic balance between mechanical stretching, capillary thinning and the timing of filament breakup. We then discuss the implications of this balance in terms of predicting breakup times for different fluids under different stretching conditions, using the breakup of magma during volcanic eruptions as a purely illustrative example.

2. Theoretical background and literature synthesis

In our experiments, and in many natural and industrial examples, stretched fluids experience capillary thinning and mechanical thinning simultaneously. In this section, we outline each process independently, drawing on experimental and theoretical results from the literature. We then present the characteristic time scales of filament stretching and breakup, which we use to scale our experimental results.

2.1. Capillary thinning of fluid filaments

The thinning of Newtonian fluid filaments under capillary forces has been thoroughly investigated in the context of extensional rheology, and capillary thinning experiments are a viable method of

measuring the extensional viscosity of Newtonian fluids [14,15]. Capillary thinning experiments begin with a small volume of fluid held between two circular, parallel plates, which are then separated rapidly to a specified distance to create an approximately cylindrical filament between them, which then thins solely under capillary forces. Newtonian fluid filaments thin at a constant rate determined by their shear viscosity μ and surface tension σ, so that

$$\frac{dR(t)}{dt} = -\left[\frac{(2X-1)}{6}\right]\frac{\sigma}{\mu}, \tag{2.1}$$

where R is the filament radius, t is time and X is a constant. Specifically, X is the ratio of the net tensile force within the filament to the force arising from capillary pressure [14]. The value of X depends on the dynamical regime studied; for example, in cases where inertia is significant, $X = 0.5912$ [21], whereas in cases where viscous forces are dominant, $X = 0.7127$ [22]. Capillary thinning experiments on Newtonian fluids with shear viscosities greater than approximately 1 Pa s are best described by the Papageorgiou [22] solution [14,15].

Equation (2.1) can be rewritten in the simpler form,

$$\frac{dD}{dt} = 2\alpha\frac{\sigma}{\mu}, \tag{2.2}$$

which uses filament diameter D and constant α in place of the term in square brackets in equation (2.1). For the Papageorgiou [22] solution, which describes the thinning of Newtonian fluids in the viscous regime, $\alpha = 0.0709$.

2.2. Mechanical thinning of fluid filaments

The fluid filament has a fixed diameter at its contacts with the endplates, so when the plates start moving apart, the filament must narrow at its mid-plane to conserve mass. The mechanical separation of the plates therefore leads to thinning that is independent of the fluid's viscosity. As such, we introduce the term 'mechanical thinning' to refer to the thinning induced by mechanical plate separation. FiSER experiments are underpinned by the concept of plate separation governing the stretching and thinning of fluids, and as such, this mode of thinning has been extensively modelled (e.g. [13,23,24]). Mechanical thinning for a fluid held between two circular, parallel plates is described by the model of Spiegelberg *et al.* [12], which we present here as

$$D(t) = D_0\left(\frac{H(t)}{H_0}\right)^{-\frac{3}{4}}, \tag{2.3}$$

where H is the height of the filament, i.e. the distance between the plates, and the subscript 0 denotes values at the start of the experiment, at $t = 0$ s, before the plates start moving apart. If the separation velocity of the plates is constant, $H(t) = H_0 + vt$, where v is the separation velocity. Therefore, we can rewrite equation (2.3) as

$$D(t) = D_0\left(1 + \frac{vt}{H_0}\right)^{-\frac{3}{4}}. \tag{2.4}$$

We then find the mechanical thinning rate as a function of time by differentiating equation (2.4) with respect to t and find that

$$\frac{dD}{dt} = -\frac{3}{4}\frac{v}{H_0}D_0\left(1 + \frac{vt}{H_0}\right)^{-\frac{7}{4}}. \tag{2.5}$$

So, for plates moving apart at a constant speed, the mechanical thinning rate decreases over time. This contrasts with the rate of capillary thinning, which is constant (equation (2.2)).

Equation (2.4) demonstrates that the mechanical thinning of a filament is governed by the initial dimensions of the fluid and by the plate separation rate. As such, our experimental results must be scaled by the plate diameter D_0 and initial separation distance H_0 to apply the findings to natural examples.

2.3. Time scales of fluid thinning and breakup

There are several time scales and deformation rates associated with extensional thinning and breakup. First, let us consider the extensional strain rate experienced by the fluid. We assume that once the fluid is sufficiently stretched, most of the filament adopts a broadly cylindrical form with a uniform diameter. The extensional strain rate $\dot{\gamma}$ of this cylindrical filament is then

$$\dot{\gamma} = -\frac{2}{D}\frac{dD}{dt}, \tag{2.6}$$

where D is the filament diameter and t is time [12,25]. FiSER experiments produce a constant extensional strain rate at the filament mid-plane by separating the plates at a specified, increasing rate (e.g. [13,24]). Capillary thinning experiments with Newtonian fluids produce a constant thinning rate, which leads to an increasing extensional strain rate at the filament mid-plane. In our experiments, where the plates move apart at a constant velocity, extensional strain rates vary: when mechanical thinning is dominant, the extensional strain rate will decrease over time, whereas if capillary thinning is dominant, the extensional strain rate will increase over time.

Now, let us consider the time scale governing fluid thinning. As outlined in §2.1, a narrow fluid filament will naturally thin under capillary pressure. There are two potential time scales that can characterize the rate of capillary thinning [10]. The first is the capillary instability time scale,

$$t_{cap} = \sqrt{\frac{\rho D(t)^3}{\sigma}}, \tag{2.7}$$

where ρ is the mass density of the fluid. The second is the viscous instability time scale,

$$t_{vis} = \frac{\mu D(t)}{\sigma}. \tag{2.8}$$

These two time scales characterize two different dynamical regimes: t_{cap} balances capillary forces against inertia, and t_{vis} balances capillary forces against viscous forces. The dominant time scale governing fluid thinning is the greater of the two. If $t_{vis} > t_{cap}$, viscous forces slow down the rate of thinning, making inertia insignificant, meaning that t_{vis} will govern thinning behaviour. This is the case for the fluids used in our experiments. Note that the dominant instability time scale is often quantified using the Ohnesorge number, $Oh = t_{vis}/t_{cap}$, where $Oh \gg 1$ indicates that thinning is in the viscous-dominated regime [6,10,26].

2.4. Previous work using plates with a constant velocity

Previous fluid extension experiments that separated the plates at a constant rate all used low-viscosity fluids dominated by inertial and gravitational effects [27–32]. These studies mostly focused on the evolving shape and internal fluid flow of the filament, rather than on breakup. Zhang *et al.* [29] measured the final length of the filament at breakup and found that it depends on a balance between fluid viscosity and surface tension, where final breakup length is increased by increasing viscosity or decreasing surface tension. However, the timing of breakup in these experiments is heavily influenced by inertial and gravitational effects.

2.5. Critical Deborah number

Experiments by Jones *et al.* [6] also investigated the breakup of Newtonian fluids between plates separated at a constant rate. Jones *et al.* [6] introduced a modified Deborah number, De^*, to characterize conditions of fluid breakup, defined as

$$De^* = \frac{\lambda_{inst}}{\lambda_d}, \tag{2.9}$$

where λ_{inst} is the dominant instability time scale governing the rate of fluid thinning and λ_d is the reciprocal of the fluid deformation rate (equation (2.6)). Therefore, De^* quantifies the balance between the capillary thinning rate and the overall thinning rate, which is a combination of mechanical and capillary thinning. Jones *et al.* [6] observed that filaments broke at a critical value of $De^*_{crit} = 0.3$. Here, we briefly explore the physical meaning of this observation, as it will inform the interpretation of our experimental observations.

First, let us consider how De^* changes throughout an experiment. When the plates move apart at a constant rate, mechanical thinning rates will decrease over time (equation (2.5)), leading to a decreasing extensional strain rate (equation (2.6)). This means that while mechanical thinning is dominant, the value of De^* will decrease as an experiment progresses.

Second, let us consider the value of De^*_{crit}. There will come a point in every stretching experiment where capillary thinning will dominate over mechanical thinning, as the rate of the rate of capillary thinning remains constant over time (equation (2.2)), while the rate of mechanical thinning decreases (equation (2.5)). Once mechanical thinning becomes insignificant, the filament will thin at a constant rate determined by capillary forces. At this point, filament diameter becomes a simple linear function of time, so that

$$D(t) = \frac{dD}{dt}(t_c - t) = 2\alpha\frac{\sigma}{\mu}(t_c - t), \tag{2.10}$$

where t_c is the time at which filament breakup occurs. By substituting equation (2.10) into equation (2.6), we find that the extensional strain rate is also a function of time, so that

$$\dot{\gamma}(t) = \frac{2}{D(t)}\frac{dD}{dt} = \frac{2}{(t_c - t)}. \tag{2.11}$$

As outlined in §2.3, the dominant time scale governing capillary thinning is t_{vis} (equation (2.8)). By substituting equation (2.10) into equation (2.8), we find that t_{vis} is also a function of time, so that

$$t_{vis} = \frac{\mu D(t)}{\sigma} = 2\alpha(t_c - t). \tag{2.12}$$

Finally, when we substitute equations (2.11) and (2.12) into equation (2.9), calculating De^* for the capillary-dominated thinning regime, we find that

$$De^*_{cap} = \frac{\lambda_{inst}}{\lambda_d} = \frac{t_{vis}}{\left(\dot{\gamma}^{-1}\right)} = \frac{2\alpha(t_c - t)}{0.5(t_c - t)} = 4\alpha. \tag{2.13}$$

So, the value of De^* in the final stages of an experiment, when capillary forces dominate, is a constant, which here we term De^*_{cap}. Using the Papageorgiou [22] similarity solution for the thinning of a Newtonian filament in the absence of inertia, where $\alpha = 0.0709$, we find that $De^*_{cap} = 0.3$, which matches the critical value identified by Jones *et al.* [6]. Therefore, the physical meaning of their observed critical value is that the stretching experiments had all entered a regime in which thinning was dominated by capillary forces, rather than by mechanical forces, in the moments immediately before breakup.

We have provided a new, physical basis for the observations of Jones *et al.* [6]. In this new context, their results demonstrate that fluid breakup is eventually always dominated by capillary forces, even if mechanical forces were dominant in the early stages of an experiment. However, some of the experiments by Jones *et al.* [6] did not break up before the plates stopped moving, meaning that their true De^*_{crit} could not be calculated. Furthermore, some of their experiments were in the inertial regime where $t_{cap} > t_{vis}$. Our experiments here greatly improve these results, as we use a camera with a higher frame rate, and our apparatus allows greater plate separation distances and more control over separation speeds, giving us greater insight into the balance between mechanical and capillary thinning forces approaching breakup.

3. Materials and methods

3.1. Fluid properties

We use four Newtonian fluids in our experiments: three polybutene silicone oils with different viscosities, which we name S1, S2 and S3, and an additional polydimethylsiloxane (PDMS) silicone oil, which we name S4. We have used fluids S1–S3 in other experiments published previously, and full details of our methods and results are available in Allgood & Jones [15]. For this study, we measured S4 following the same methods, summarized here. The shear viscosity of the fluid was measured using an Anton Paar MCR702e rotational rheometer with a cone-and-plate geometry, using a 1° cone with a diameter of 25 mm and cone truncation of 51 µm. A full rheological characterization of fluids S1–S4 is presented in the electronic supplementary materials.

Table 1. Properties of four Newtonian silicone oils, with one standard deviation provided beside mean values from repeat experiments.

fluid	composition	shear viscosity μ at 20°C (Pa s)	density ρ at 20°C (kg m^{-3})	surface tension σ (mN m^{-1})
S1	polybutene	0.86 ± 0.01	838.7 ± 2.9	30.76 ± 0.74
S2	polybutene	6.9 ± 0.08	842.2 ± 2.9	28.65 ± 2.17
S3	polybutene	64 ± 0.38	908.4 ± 3.0	27.24 ± 1.98
S4	PDMS	14 ± 0.09	976.0 ± 3.0	16.61 ± 1.05

S1–S3 are all Newtonian, and at 20°C they have viscosities of 0.86, 6.9 and 64 Pa s, respectively [15]. S4 is broadly Newtonian but displays very weak shear-thinning behaviour. Its viscosity is constant at 13.7 Pa s below a shear rate of 30 s^{-1}, but decreases to 13.5 Pa s at 100 s^{-1} (fig. A1, electronic supplementary material). The viscosity–temperature relationships of the four silicone oils in the range 10 to 30°C are best approximated by Arrhenius-style model fits of the form $\log(\mu) = \log(A) + B/T$, where A has units Pa s and B has units K. We derive the relationships:

$$\log(\mu_{S1}) = -18.381 + \frac{5340.0}{T}, \tag{3.1a}$$

$$\log(\mu_{S2}) = -17.522 + \frac{5706.0}{T}, \tag{3.1b}$$

$$\log(\mu_{S3}) = -21.827 + \frac{7619.5}{T}, \tag{3.1c}$$

$$\log(\mu_{S4}) = -2.7863 + \frac{1582.4}{T}, \tag{3.1d}$$

where μ is shear viscosity in Pa s, T is temperature in K and the subscript denotes the silicone oil. Equations (3.1a)–(3.1c) are from Allgood & Jones [15], and equation (3.1d) is from new data for S4 (electronic supplementary material, fig. A2). These equations are needed to calculate the precise viscosity of the fluid based on its temperature.

The density–temperature relationships for the four silicone oils in the range 15–25°C are approximately linear, with lines of best-fit of the form $\rho = \rho_r (1 + b\,(T - 293.15))$, where ρ is the fluid density in kg m^{-3}, T is the fluid temperature in K, ρ_r is the fluid density at 20°C (293.15 K) interpolated from the lines of best fit and b is the coefficient of volume expansion in K^{-1}. We find that

$$\rho_{S1} = 838.64(1 - 0.00081978(T - 293.15)) \pm 2.9, \tag{3.2a}$$

$$\rho_{S2} = 842.20(1 - 0.0010956(T - 293.15)) \pm 2.9, \tag{3.2a}$$

$$\rho_{S3} = 908.40(1 - 0.0028823(T - 293.15)) \pm 3.0, \tag{3.2c}$$

$$\rho_{S4} = 976.04(1 - 0.0012792(T - 293.15)) \pm 3.0. \tag{3.2d}$$

We display compound uncertainties associated with the method, outlined in detail in Allgood & Jones [15]. New density data for fluid S4 are presented in fig. A3 in the electronic supplementary materials. Density–temperature relationships are needed to calculate the precise density of the fluid based on its temperature, to quantify the extent of gravitational sagging. Surface tensions σ were measured using the pendant drop method, as outlined in Allgood & Jones [15], and the surface tensions of all four silicone oils at room temperature (19–22°C) are listed in table 1 along with a summary of the other fluid physical properties.

3.2. Filament stretching apparatus

Our filament stretching apparatus is a TriMaster extensional rheometer, equipped with two smooth, circular, stainless steel plates, which move at equal and opposite velocities to a specified separation distance. The device uses a stepper motor and a drive belt to move the plates at specified velocities. Experiments are recorded by a high-speed Chronos camera at 1000 frames per second, targeted at the vertical mid-plane of the fluid filament, exactly halfway between the moving plates (figure 1). The filament is illuminated through a light diffusion sheet, which ensures that images have a background of constant brightness, required for automated image analysis.

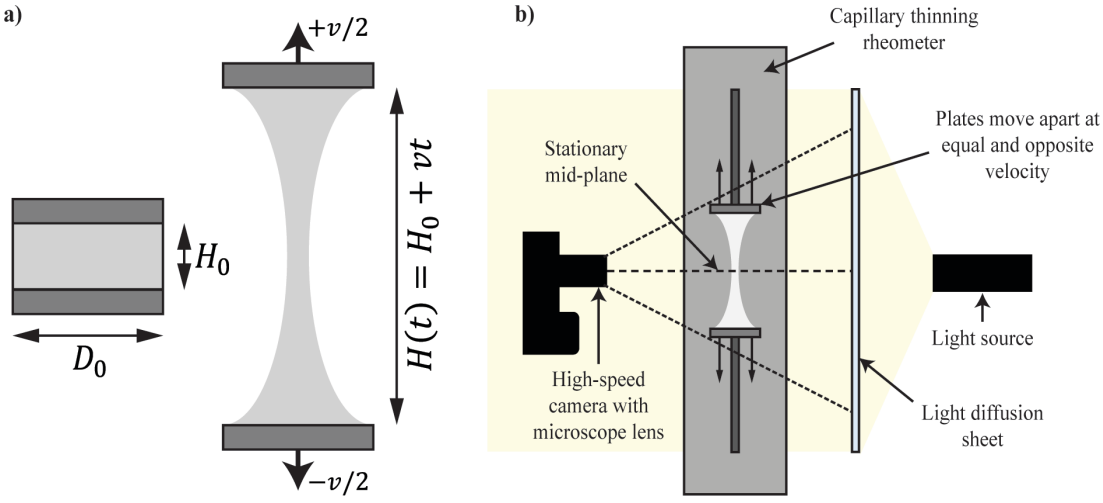

Figure 1. Schematic diagram of our experimental set-up: (a) the initial, cylindrical configuration of fluid between the plates at time $t = 0$, with aspect ratio H_0/D_0, and the dynamic configuration at $t > 0$, when the plates are moving apart at equal and opposite velocities v; (b) arrangement of the high-speed camera, focused on the fluid mid-plane, and the light source with the diffusion sheet.

We use two sets of plates, with diameters of 1 and 2 mm. The plate diameter determines the initial diameter of the fluid column, D_0 (figure 1*a*). We use plate diameters of 1 and 2 mm in order to limit gravitational sagging, which would otherwise cause fluid to flow down towards the lower plate, adding an additional stretching force to the thread. The effect of gravitational sagging is commonly characterized by the dimensionless Bond number:

$$Bo = \frac{\rho g R^2}{\sigma}, \tag{3.3}$$

where g is gravitational acceleration. Our experiments all begin with $Bo < 1$. However, Bo does not capture the effect of initial fluid height, H_0, which we find has a significant influence on the amount of gravitational sagging. We therefore only used initial fluid aspect ratios less than 0.6, in order to limit gravitationally driven flow. We also only used initial aspect ratios H_0/D_0 greater than 0.05 in order to avoid creating Saffman–Taylor instabilities when the plates are separated, and because smaller volumes of fluid produce much shorter experiments, limiting our ability to identify trends in the mid-plane diameter data.

An experiment begins with fluid held between the two plates. We ensure that the fluid has an initially cylindrical form at $t = 0$ s (figure 1*a*), which makes it straightforward to predict mechanical thinning using equation (2.4). This cylindrical form is created by placing a droplet on the lower plate, then moving the plates together so that the liquid forms a bridge between them. Once the fluid has spread to wet the entire surface of each plate, the plate separation is adjusted manually to bring the fluid into a perfect cylindrical form. The plates are then separated at a constant, specified velocity. We use separation velocities between 2 and 150 mm s^{-1} and conduct repeat experiments at 2, 4, 8, 16, 32, 50, 100 and 150 mm s^{-1} to account for the variation in H_0. We know from equation (2.4) that a greater value of H_0, i.e. a greater volume of fluid, will take longer to thin and break. Once the fluid has broken and the plates stop moving, we measure the temperature of the fluid. This allows us to calculate the fluid viscosity and density for each experiment using equations (3.1) and (3.2), respectively, so that we can account for slight variations in laboratory temperature, which was between 18.4°C and 23.7°C. A list of all experiments is provided in table A1 in the electronic supplementary materials.

3.3. Image analysis

First, we identify the frame in which the plates start moving and the frame in which the filament breaks (figure 2). These frames provide the total duration of an experiment, i.e. the breakup time of the fluid. The images are then analysed in MATLAB, with the filament width measured based on brightness differences between the fluid and the background. We find that the brightness-based automated image analysis is reliable until the filament reaches a width of five pixels, so the automated

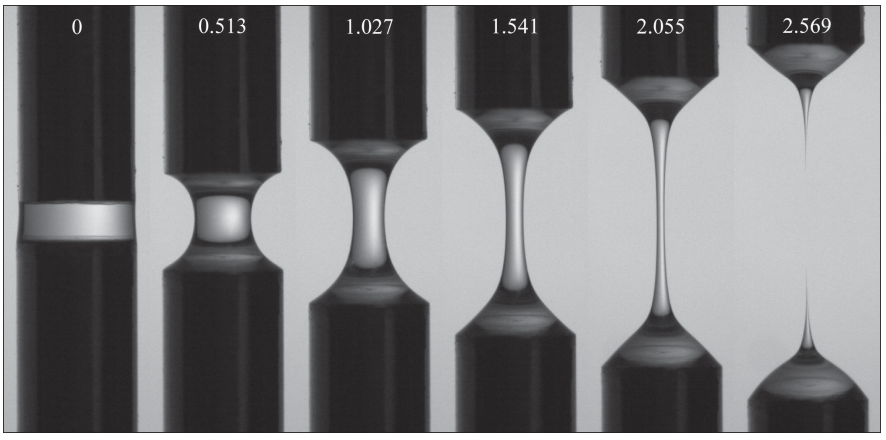

Figure 2. Image frames from a filament stretching experiment on fluid S4, with 2 mm diameter plates moving apart at 2 mm s^{-1}. Times are shown in seconds. The filament broke at 2.569 s, the last image frame shown here.

analysis is ended once the filament reaches this width. A validation of the automated measurements against manual width measurements is presented in fig. A4 in the electronic supplementary materials.

We also use the high-speed video frames to track the plate positions and calculate plate separation velocity, which is a key parameter for understanding mechanical thinning (§2.2). We find that the plates move at a constant velocity (electronic supplementary materials, fig. A5), with only minor acceleration effects in the initial stages, particularly for lower specified plate separation rates. When calculating mechanical thinning (equation (2.3)), we use the recorded plate positions to find H. If the plates move beyond the camera field of view, $H(t)$ is then calculated based on the last measured plate separation and the measured velocity of the plates.

4. Results and analysis

4.1. Breakup time

We find that the breakup time of a fluid filament is a function of the plate separation rate υ, initial fluid aspect ratio H_0/D_0 and the ratio of viscosity to surface tension μ/σ (figure 3*a*). The data collapse onto a single curve when breakup times are normalized against the viscous instability time scale of the fluid, t_{vis} (equation (2.8)), and plate separation velocities are normalized against t_{vis} over the initial height of the fluid, H_0 (figure 3*b*). We note that the normalized velocity, $\upsilon_n = \upsilon t_{vis}/H_0$, is equivalent to the capillary number Ca used by Kröger & Rath [28] and is equal to the proportional increase in filament height attained in t_{vis}. This normalization demonstrates the strong relationship between breakup time and plate separation velocity. The equation for the line of best fit has the form of a simple power law,

$$\frac{t_{brk}}{t_{vis}} = A\left(\frac{\upsilon\, t_{vis}}{H_0}\right)^B, \tag{4.1}$$

which can be rearranged to

$$t_{brk} = A\left(\frac{H_0}{\upsilon}\right)^{-B}\left(\frac{D_0\mu}{\sigma}\right)^{B+1}, \tag{4.2}$$

by substituting equation (2.8). This demonstrates that the breakup time depends on both the plate separation time scale H_0/υ and the viscous instability time scale $D_0\mu/\sigma$.

Although most of our data fall on a single curve, we note that the data from the lowest viscosity silicone oil, S1, at the lowest plate separation rates, deviate from the trend (red symbols; figure 3*b*). Filaments under these conditions broke up later than anticipated, and we suggest that this relates to the low normalized plate separation velocity leading to a violation of the assumptions of the Papageorgiou [22] solution. We discuss this further in the following section.

Based on our experiments, we find that $A = 3.81$ and $B = -0.44$. These values were generated by fitting a power law through the data for which $\upsilon_n > 1$, from four Newtonian silicone oils with a range of viscosities and surface tensions, and from 1 and 2 mm diameter plates. We have therefore established

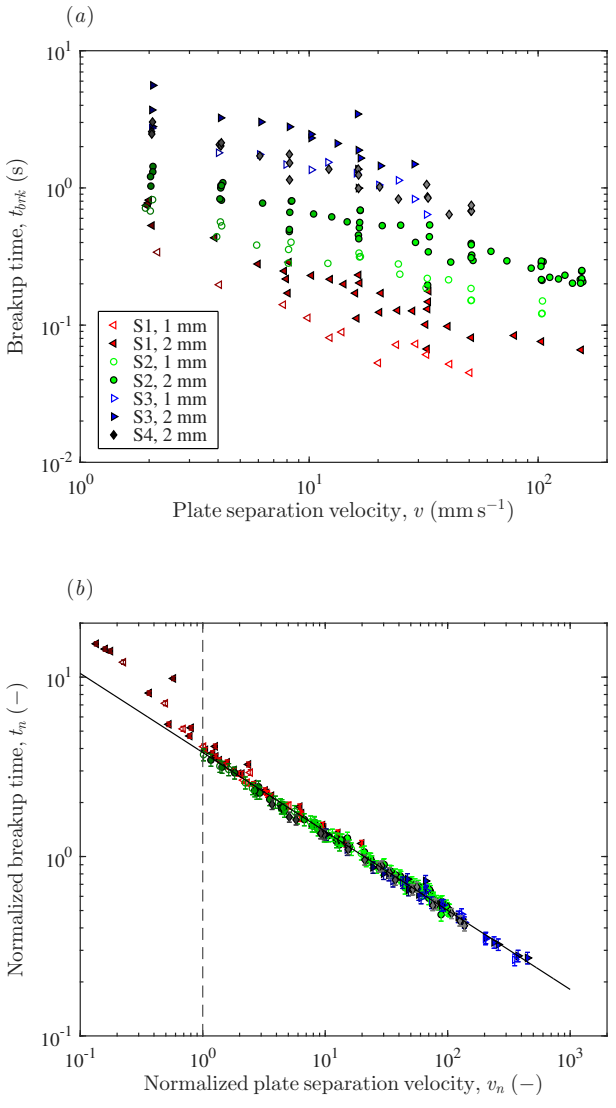

Figure 3. Breakup times of stretched silicone oil filaments between plates separated at a constant velocity. (*a*) Raw data for filament breakup time t_{brk} and plate separation velocity υ. (*b*) Normalized breakup time $t_n = t_{brk}/t_{vis}$ against normalized plate separation velocity $\upsilon_n = \upsilon\, t_{vis}/H_0$, with the data collapsing onto one curve. Vertical dashed line shows a break in slope at a normalized plate separation velocity of one. Error bars include the uncertainty associated with surface tension data and in most cases are smaller than the data points. The legend lists the fluid used (S1–S4) followed by the plate diameter.

an empirical relationship between fluid properties μ and σ, initial fluid conditions D_0 and H_0, and plate separation rate υ, which should be applicable to the breakup of all Newtonian fluids in the viscous thinning regime, stretched at a constant rate, and with insignificant gravitational effects. However, the dynamics behind this simple empirical relationship are complex, and we explore them in the following section.

4.2. Balance between mechanical- and capillary-dominated thinning

The balance between mechanical- and capillary-dominated thinning can be seen by tracking the decrease in the filament mid-plane diameter over time. In every experiment, thinning rates are highest in the instant the plates start moving (figure 4). In the initial stages, thinning is dominated by mechanical forces, with measured diameters in close agreement with equation (2.4) from Spiegelberg *et al.* [12] (see dashed lines in figure 4). Then, in the intermediate stage, the observed thinning rate exceeds the mechanical thinning rate, as capillary thinning starts to become significant. In the final stage, as the fluid approaches breakup, the observed rate of thinning approaches the capillary thinning rate

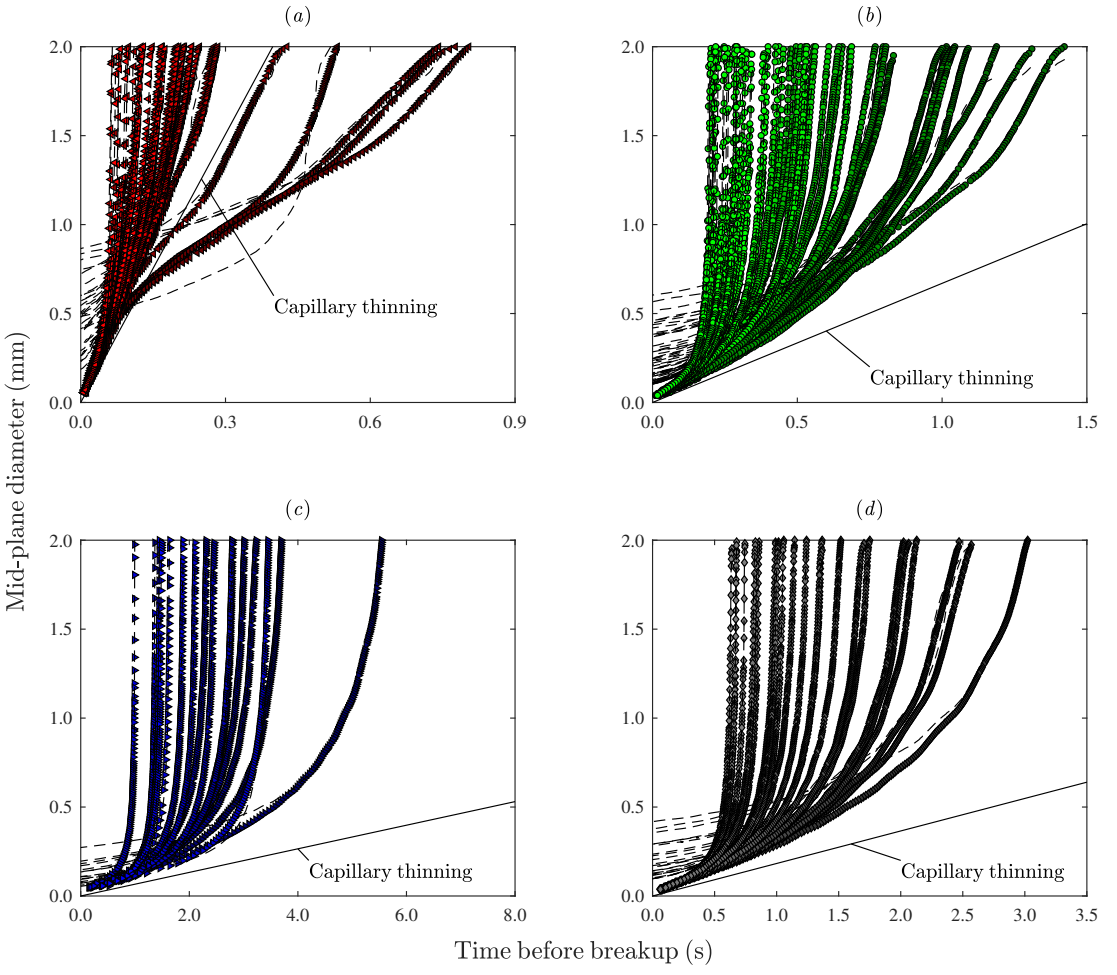

Figure 4. Evolution of filament mid-plane diameters throughout fluid stretching experiments on the 2 mm diameter plates: (*a*) S1, (*b*) S2, (*c*) S3 and (*d*) S4. To aid visualization, points show the median time at which each filament mid-plane diameter was observed, rather than showing every measurement at 1000 frames per second. Dashed lines show mechanical thinning calculated forwards from initial conditions, as described by equation (2.4) [12], and solid lines show capillary thinning calculated backwards from fluid breakup, as described by equation (2.2) [22], using mean fluid viscosities from the experiments shown.

predicted by equation (2.2) from Papageorgiou [22] (see solid lines in figure 4), showing that capillary thinning has become dominant.

The intermediate stage of an experiment marks the transition from mechanical- to capillary-dominated thinning. In this stage, the overall thinning rate is greater than either mechanical or capillary thinning in isolation, as both processes are acting simultaneously. The only experiments in which this is not the case are the low-viscosity, low-velocity runs previously highlighted as outliers (§4.1, figure 3*b*).

For the low-viscosity, low-velocity case ($\upsilon_n < 1$), thinning is initially dominated by mechanical forces, despite the mechanical thinning rate being slower than the theoretical capillary thinning rate (figure 4*a*). This happens for two reasons. First, capillary thinning will only occur once the filament height $H(t)$ exceeds a critical threshold H_{crit}, and for a slow plate separation rate, it takes a significant amount of time to reach this threshold. For a perfectly cylindrical fluid column, $H_{crit} = 2\pi R_0$ [7,29], but for the fluids in our experiments, which are not cylindrical owing to necking at their mid-plane, $H_{crit} < 2\pi R_0$. Second, once $H(t) \geq H_{crit}$ and capillary forces become significant, the strongly necked filament profile will not match the assumptions of the Papageorgiou [22] solution. Indeed, for the slowest plate separation rates, we observe that thinning is slower than the Papageorgiou [22] solution for most of the experiment and that it only becomes faster than the Papageorgiou [22] solution immediately prior to breakup (figure 4*a*). Clearly, there is a lower limit to when the Papageorgiou [22] solution can be applied, and based on the change in slope in figure 3*b*, this appears to be at $\upsilon_n \sim 1$.

For all other cases ($\upsilon_n > 1$), mechanical thinning is rapid enough that $H(t)$ exceeds H_{crit} almost instantaneously, and the resulting long, narrow thread closely resembles the shape assumed by the Papageorgiou [22] solution. As such, the thinning rate gradually approaches the theoretical capillary

thinning rate (equation (2.2)). From here, we focus our analysis on cases where $\upsilon_n > 1$, as these are the most likely to produce long, thinning threads.

There is no straightforward way to predict the thinning rate through the intermediate stage of an experiment. As soon as capillary thinning becomes significant, fluid is redistributed within the filament, moving from the narrow central thread into the wider reservoir regions at the endplates, at which point the mechanical thinning model (equation (2.4)) no longer applies. Predicting the transition from mechanical- to capillary-dominated thinning would probably require a computational dynamical model, which is beyond the scope of this study. However, it is clear from our data that the transition from mechanical- to capillary-dominated thinning follows a consistent pattern, which we explore further in the following subsection.

4.3. Universal breakup behaviour

There is a strong correlation between the normalized plate separation velocity and the normalized breakup time (figure 3*b*). The filament breakup time is probably the time scale of greatest interest for most natural or industrial problems; however, it provides relatively little information about the thinning process itself. To understand the evolution of filament diameter, we combine figures 3 and 4 into a three-dimensional plot, mapping the change in normalized filament mid-plane diameter D/D_0 over normalized time $t_n = t/t_{vis}$. We find that the data from all four fluids collapse onto a single surface (figure 5). In this context, the breakup times in figure 3*b* represent a slice through this surface at $D/D_0 = 0$.

The surface in figure 5 demonstrates that Newtonian fluid filaments, stretched at a constant velocity, thin in a universal manner. All thinning profiles fall on this surface, with their precise position determined by the normalized plate separation velocity υ_n, which incorporates fluid viscosity, surface tension, initial column height and plate separation rate. Scatter in the data increases towards $D/D_0 = 1$ owing to plate movement being more irregular in the initial, short-lived acceleration phase. Once the plates attain a constant velocity, later in the thinning process and for smaller values of D/D_0, the scatter in the data reduces, especially once capillary thinning becomes dominant, lessening the influence of mechanical plate movement.

The shape of the surface is complex. When $D/D_0 = 1$, the normalized time t_n must equal zero by definition. Then, as soon as the plates start moving and $t_n > 1$, there is a large divergence in behaviour. In the $\upsilon_n \ll 1$ regime, the surface has a convex profile, with thinning rates that increase as thinning progresses. This type of behaviour can be seen in figure 4*a*, for the experiments in which initial thinning rates are less than theoretical capillary thinning rates, and the shape of the fluid filament never satisfies the assumptions of the Papageorgiou [22] solution. In the $\upsilon_n \gg 1$ regime, the surface has a concave profile, with thinning rates decreasing as thinning progresses. This is the most common behaviour observed in our experiments (e.g. figure 4*b–d*), where the filament eventually thins in accordance with the Papageorgiou [22] capillary thinning solution.

5. Discussion

5.1. Predicting filament breakup times and maximum lengths

We have developed an empirical equation that allows the breakup time of Newtonian fluids, stretched by plates moving at a constant velocity, to be predicted from fluid properties, initial conditions and plate velocity. Equation (4.2) applies to all Newtonian fluids that thin in the viscous regime ($t_{vis} > t_{cap}$, §2.3), and for which the normalized plate separation velocity $\upsilon_n \gtrsim 1$.

However, there are limitations to the equation. First, it does not account for the gravitational slumping which can occur once the filament is sufficiently long. Long threads are particularly likely for high-viscosity, high-velocity runs, and these threads are susceptible to slumping downwards under their own weight, often pulling sideways when they destabilize. Gravitationally driven flow is not significant early in the experiment, as evidenced by our experimental filaments remaining symmetrical about their mid-plane. However, as a filament gets longer and narrower, its weight is focused onto a smaller cross-sectional area, and although this 'hydrostatic' pressure is initially counteracted by capillary pressure and plate movement, it can increase until the filament destabilizes under its own weight. Slumping and destabilization would be even more disruptive if the filament was stretched horizontally. Another complicating factor is that long-lasting, high-viscosity filaments are vulnerable

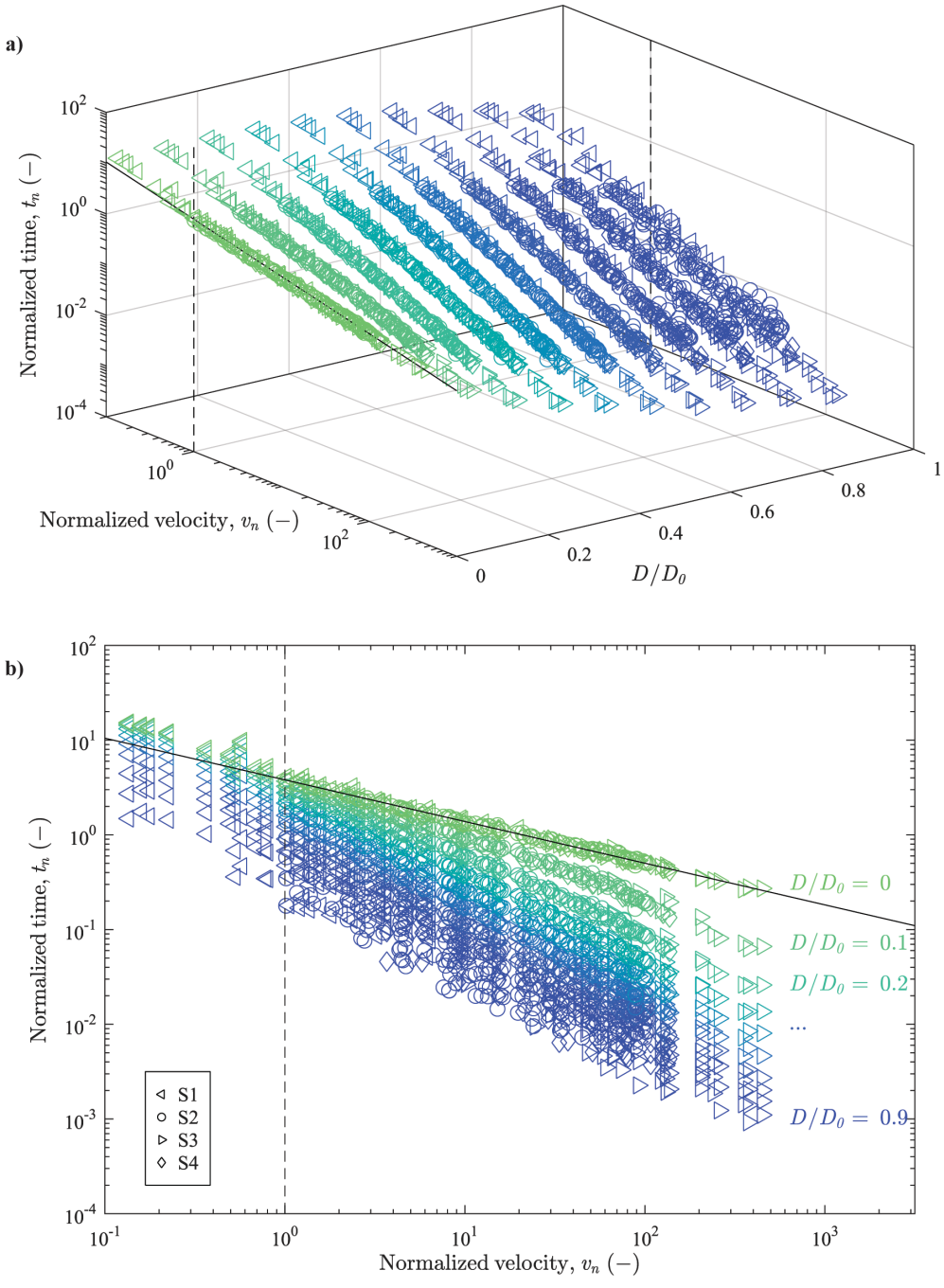

Figure 5. Thinning profiles for all experiments collapse onto a single surface, shown here in three dimensions (a) and two dimensions (b) as a series of normalized times $t_n = t/t_{vis}$ at normalized diameters D/D_0. The points in the plane $D/D_0 = 0$ show the normalized breakup time of the experiments, equivalent to the data in figure 3*b*. The solid black line shows the best-fit power law for breakup discussed in §4.1, and the vertical dashed line at $v_n = 1$ highlights the break in slope identified in figure 3*b*. Marker colour indicates normalized diameters in increments of 0.1, as labelled in (b).

to being disrupted by air movements around them, which will again lead to breakup sooner than predicted by equation (4.2).

5.2. Magma breakup example

We now apply our experimental findings to a natural case: the breakup of basaltic magma clasts ejected from a mildly explosive volcanic eruption. We intend this to be a purely illustrative example

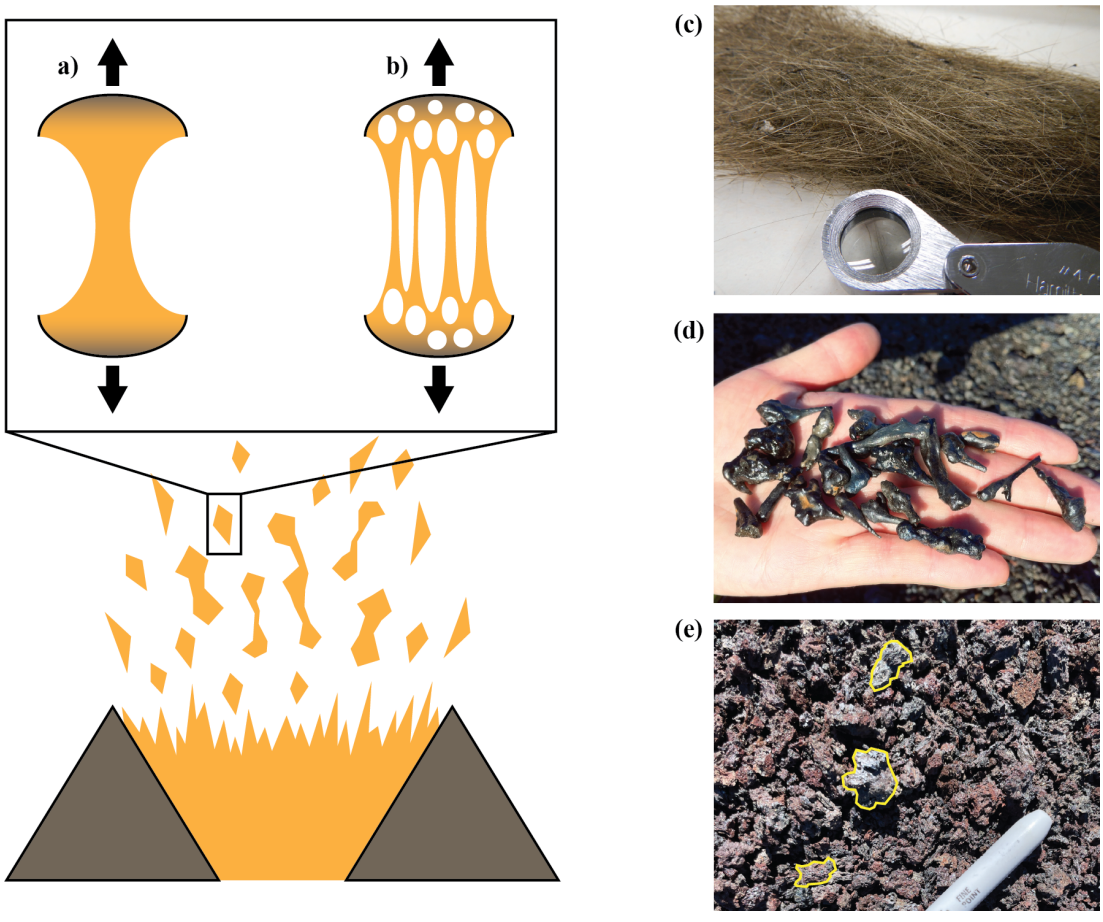

Figure 6. Formation of lava filaments during an explosive basaltic eruption. Schematic cartoon showing the stretching of ejected, airborne pyroclasts: (a) a bubble-free pyroclast and (b) a bubbly pyroclast producing multiple narrow filaments. Photos of volcanic products: (c) narrow filaments of solidified lava known as Pele's hair, with a hand lens for scale [Cm3826, CC BY-SA 4.0 <https://creativecommons.org/licenses/by-sa/4.0>,via Wikimedia Commons]; (d) stretched, solidified droplets known as Pele's tears [Ivtorov, CC BY-SA 4.0 <https://creativecommons.org/licenses/by-sa/4.0>, via Wikimedia Commons]; (e) solidified fragments known as scoria, with three fragments outlined for clarity, and the end of a pen shown for scale.

of how an understanding of fluid breakup can inform and advance our understanding of natural processes.

Basaltic magma is relatively low-viscosity within the suite of naturally occurring magmas and is commonly associated with lava fountains or jets, as seen on Hawaii or in Iceland (e.g. [33–35]). The breakup dynamics of the magma control the formation of fluid filaments and droplets, which then solidify into material known as tephra (figure 6). The size and shape of tephra fragments determine the nature of hazards posed in an eruption; for example, smaller fragments can be carried farther by the wind and can cause a greater respiratory or aviation risk. As such, it is of great importance to volcanologists to understand how eruption conditions can change the breakup behaviour of lava.

Two of the fluids used in our experiments are directly comparable to the pure melt (i.e. liquid) phase of magma. We assume that basaltic magmas have viscosities ranging from 100 to 10 000 Pa s [36], with surface tensions of 0.1–0.3 N m^{-1} [37–39], and densities of 2500–2800 kg m^{-3} [36]. As such, the thinning of these magmas will be dominated by the viscous instability time scale (equation (2.8)), like the fluids used in our experiments. Furthermore, fluids S3 and S4 have ratios of surface tension to viscosity within the likely range of basalt (figure 7). We note that natural magma will contain crystals and bubbles that, depending on their abundance, may modify its rheology [40] and influence the thinning process; however, we only intend this as an illustrative example.

Based on our experiments, we can predict the breakup time for a cylinder of basaltic melt held between two plates separated at a constant rate. In the natural environment, we must imagine that the 'plates' are merely the extremities of a launched ballistic projectile, commonly known as a volcanic 'bomb' (figure 6). In eruptions on Etna and Stromboli, 21% of centimetre- to decimetre-sized bombs have been observed to be 'bilobate', i.e. in the process of stretching apart to produce a thin filament

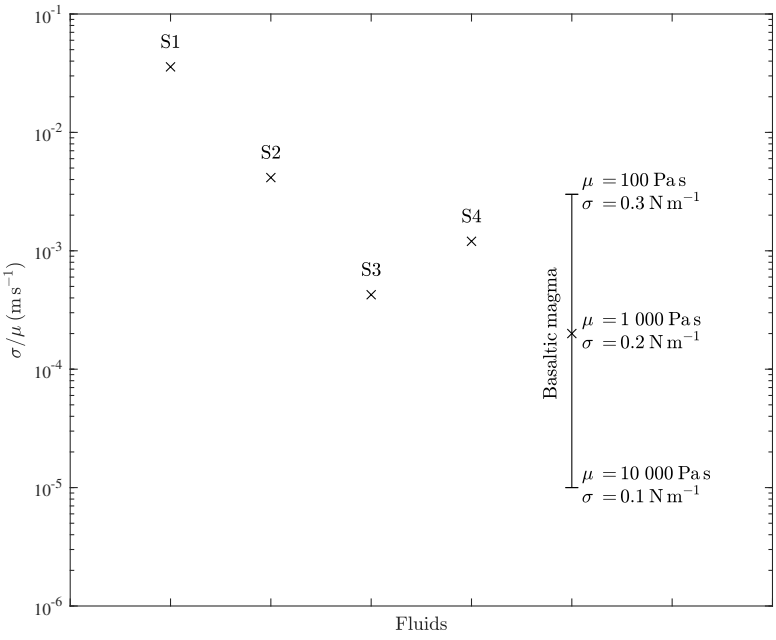

Figure 7. Comparison of the ratios of surface tension σ (N m^{-1}) to viscosity μ (Pa s) for the four Newtonian fluids used in this study (S1–S4) and the likely natural range of basaltic magma. The ratio yields a fluid thinning rate in m s^{-1} (equation 2.2).

between bulbous ends [41]. As an example, we consider a cylindrical volume of magma 5 cm in diameter and 2.5 cm in height. At a viscosity of 100 Pa s, this volume would attain a maximum filament length of 0.9–1.3 m before breaking up, when stretched at 5 cm s^{-1}. At a higher viscosity of 1000 Pa s, and at separation velocities greater than 1 m s^{-1}, the theoretical maximum length is tens of metres. However, such long, thin filaments would be very vulnerable to air currents and gravitational sagging encouraging breakup.

Our experiments thus validate and quantify the intuitive assumption that a greater stretching rate leads to longer filaments and a faster breakup, and that higher viscosities lead to longer filaments and a slower breakup. For magma being deformed in-flight, the rate of breakup is also in competition with the rate of solidification; if a magma filament breaks into droplets while molten, the resulting clasts will look different to a filament that solidified while still being stretched. In volcanology, relating tephra shapes to fluid breakup dynamics is an ongoing area of research [6,10,42–44].

We can also consider extensional conditions at a smaller scale. If we imagine a large volcanic bomb filled with gas bubbles (figure 6*b*), we can treat the melt films between these bubbles as individual filament stretching events. Here, the starting volume of melt is much smaller, similar to the dimensions used in our experiments. A filament of initial height 1 mm and diameter 2 mm, pulled apart at 5 cm s^{-1}, would break up in 2.5–3.6 s, attaining a length of 12–18 cm. This could occur during the breakup of larger bombs, which have been observed to tear and stretch at their edges during flight [45].

Intuitively, it might seem unlikely that long, narrow filaments, up to metres in length, could be sustained in volcanic eruptions, either owing to slumping under their own weight, or owing to the wind. However, some basaltic eruptions are known to produce fibre-like tephra known as Pele's hair, demonstrating that very long, very thin magma filaments occur in nature (figure 6*c*). The preservation of these features depends on the solidification of the filament, which occurs while it is being stretched [10,11,44], and as such, not all eruptions have conditions suitable for producing Pele's hair. The relationship between filament length, solidification and resulting tephra clast shapes remains to be determined, but understanding the timing of breakup is a necessary first step.

6. Conclusion

By conducting uniaxial extension experiments on Newtonian fluids with a range of viscosities and surface tensions, we have demonstrated that filament breakup time can be reliably predicted from

initial fluid dimensions, viscosity, surface tension and the plate separation rate. Data can be normalized to collapse onto a single curve, yielding an empirical power-law equation that may be used to calculate breakup times (equation (4.2)), or equivalently, maximum filament lengths. This empirical equation can be used in all cases where $\upsilon_n = \upsilon t_{vis}/H_0 \gtrsim 1$, and where the filament does not slump under its own weight or face disruption from air currents.

We also find that the evolution of the filament mid-plane diameter throughout each experiment is dependent on υ_n, irrespective of fluid properties or plate size. However, developing a physical model to account for the seemingly universal behaviour evidenced by our experimental data is beyond the scope of this study. As outlined in §4.2, the transition from mechanical-dominated to capillary-dominated thinning is complex, and the scenario may be viewed as a capillary thinning experiment in which the boundary conditions are constantly changing. Computational models (e.g. [29,30,32,46]) could be used to further investigate the universality of this type of thinning behaviour.

Finally, we note that equation (4.2) is unlikely to apply to non-Newtonian fluids. For example, viscoelastic fluids form long, cylindrical threads in capillary thinning experiments owing to elastic stresses increasing to counter capillary stresses, as well as sometimes forming 'beads-on-a-string' structures (e.g. [25,26]). The stabilizing effect of elastic stresses could potentially increase the lifespan of viscoelastic filaments compared to Newtonian filaments, if they were stretched under the conditions explored here, whereas the formation of beads-on-a-string could disrupt thinning and influence the shapes of droplets after breakup. Therefore, further experiments are needed to explore the applicability of equation (4.2) to non-Newtonian materials, including viscoelastic fluids, shear-thinning fluids, suspensions and emulsions.

Ethics. This work did not require ethical approval from a human subject or animal welfare committee.

Data accessibility. All raw image data, in the form of recorded mid-plane diameters and high-speed camera footage, are available on Zenodo [47].

Other raw data are provided in the supplementary materials: data for the properties of fluid S4 (electronic supplementary material, SM1); a full list of all the experiments and their conditions (electronic supplementary material, SM2); a validation of automated image analysis compared to manual measurements (electronic supplementary material, SM3); and plate movement data captured from the high-speed image recordings (electronic supplementary material, SM4) [48].

Declaration of AI use. We have not used AI-assisted technologies in creating this article.

Authors' contributions. C.A.: conceptualization, formal analysis, investigation, methodology, writing—original draft, writing—review and editing; T.J.J.: conceptualization, funding acquisition, methodology, project administration, writing—review and editing.

Both authors gave final approval for publication and agreed to be held accountable for the work performed therein.

Conflict of interest declaration. We declare we have no competing interests.

Funding. This work was supported by a UK Research and Innovation (UKRI) Future Leaders Fellowship (MR/W009781/1) awarded to Thomas J. Jones.

Acknowledgements. We would like to thank Marie Hagenbourger for advice on conducting stretching experiments with the TriMaster and using high-speed cameras, Pier Paolo Comida for assistance in measuring the density of silicone oils and Megan Long for assistance in measuring filament diameters manually in Fiji ImageJ.

References

1. Nasr GG, Yule AJ, Bendig L. 2002 Introduction to industrial sprays. In *Industrial sprays and atomization*, pp. 1–6. London: Springer London. (doi:10.1007/978-1-4471-3816-7_1)
2. Cheng X *et al*. 2025 The sea spray generation function for large droplets based on sea salt aerosol flux observation. *JGR Atmos.* **130**, e2025JD043359. (doi:10.1029/2025JD043359)
3. Villermaux E, Bossa B. 2009 Single-drop fragmentation determines size distribution of raindrops. *Nat. Phys*. **5**, 697–702. (doi:10.1038/nphys1340)
4. Kojić N, Bico J, Clasen C, McKinley GH. 2006 Ex vivo rheology of spider silk. *J. Exp. Biol*. **209**, 4355–4362. (doi:10.1242/jeb.02516)
5. Gonnermann HM. 2015 Magma fragmentation. *Annu. Rev. Earth Planet. Sci*. **43**, 431–458. (doi:10.1146/annurev-earth-060614-105206)
6. Jones TJ, Reynolds CD, Boothroyd SC. 2019 Fluid dynamic induced break-up during volcanic eruptions. *Nat. Commun*. **10**, 3828. (doi:10.1038/s41467-019-11750-4)
7. Plateau J. 1857 I. Experimental and theoretical researches on the figures of equilibrium of a liquid mass withdrawn from the action of gravity. – Third series. *Lond. Edinb. Dubl. Phil. Mag. J. Sci.* **14**, 1–22. (doi:10.1080/14786445708642346)
8. Rayleigh, Lord. 1878 On the instability of jets. Proc. London Math. Soc. **s1-10**, 4–13. (doi:10.1112/plms/s1-10.1.4)
9. Eggers J, Villermaux E. 2008 Physics of liquid jets. *Rep. Prog. Phys*. **71**, 036601. (doi:10.1088/0034-4885/71/3/036601)

10. Villermaux E. 2012 The formation of filamentary structures from molten silicates: Pele's hair, angel hair, and blown clinker. *Comptes Rendus Mécanique* **340**, 555–564. (doi:10.1016/j.crme.2012.06.003)
11. Cannata CB, De Rosa R, Donato P, Donato S, Lanzafame G, Mancini L, Houghton BF. 2019 First 3D imaging characterization of Pele's hair from Kilauea volcano (Hawaii). *Sci. Rep*. **9**, 1711. (doi:10.1038/s41598-018-37983-9)
12. Spiegelberg SH, Ables DC, McKinley GH. 1996 The role of end-effects on measurements of extensional viscosity in filament stretching rheometers. *J. Non Newton. Fluid Mech*. **64**, 229–267. (doi:10.1016/0377-0257(96)01439-5)
13. Anna SL, McKinley GH, Nguyen DA, Sridhar T, Muller SJ, Huang J, James DF. 2001 An interlaboratory comparison of measurements from filament-stretching rheometers using common test fluids. *J. Rheol*. **45**, 83–114. (doi:10.1122/1.1332388)
14. McKinley GH, Tripathi A. 2000 How to extract the Newtonian viscosity from capillary breakup measurements in a filament rheometer. *J. Rheol*. **44**, 653–670. (doi:10.1122/1.551105)
15. Allgood C, Jones TJ. 2025 Capillary thinning extensional rheometry for Newtonian fluids. *J. Rheol*. **69**, 1017–1035. (doi:10.1122/8.0001018)
16. Dinic J, Zhang Y, Jimenez LN, Sharma V. 2015 Extensional relaxation times of dilute, aqueous polymer solutions. *ACS Macro Lett*. **4**, 804–808. (doi:10.1021/acsmacrolett.5b00393)
17. Dinic J, Biagioli M, Sharma V. 2017 Pinch-off dynamics and extensional relaxation times of intrinsically semi-dilute polymer solutions characterized by dripping-onto-substrate rheometry. J. Polym. Sci. B. Polym. Phys. **55**, 1692–1704. (doi:10.1002/polb.24388)
18. Dinic J, Jimenez LN, Sharma V. 2017 Pinch-off dynamics and dripping-onto-substrate (DoS) rheometry of complex fluids. *Lab Chip* **17**, 460–473. (doi:10.1039/c6lc01155a)
19. Campo-Deaño L, Clasen C. 2010 The slow retraction method (SRM) for the determination of ultra-short relaxation times in capillary breakup extensional rheometry experiments. *J. Nonnewton. Fluid Mech*. **165**, 1688–1699. (doi:10.1016/j.jnnfm.2010.09.007)
20. Calabrese V, Shen AQ, Haward SJ. 2025 Effects of polydispersity and concentration on elastocapillary thinning of dilute polymer solutions. *Phys. Rev. X* **15**, 021025. (doi:10.1103/PhysRevX.15.021025)
21. Eggers J. 1993 Universal pinching of 3D axisymmetric free-surface flow. *Phys. Rev. Lett*. **71**, 3458–3460. (doi:10.1103/physrevlett.71.3458)
22. Papageorgiou DT. 1995 On the breakup of viscous liquid threads. *Phys. Fluids***7**, 1529–1544. (doi:10.1063/1.868540)
23. Yao M, McKinley GH. 1998 Numerical simulation of extensional deformations of viscoelastic liquid bridges in filament stretching devices. *J. Non Newton. Fluid Mech*. **74**, 47–88. (doi:10.1016/s0377-0257(97)00052-9)
24. Anna SL, Rogers C, McKinley GH. 1999 On controlling the kinematics of a filament stretching rheometer using a real-time active control mechanism. *J. Nonnewton. Fluid Mech*. **87**, 307–335. (doi:10.1016/S0377-0257(99)00072-5)
25. McKinley GH. 2005 Visco-elastic-capillary thinning and break-up of complex fluids. In *Rheology reviews* (eds DM Binding, K Walters), pp. 1–49. London: The British Society of Rheology.
26. Bhat PP, Appathurai S, Harris MT, Pasquali M, McKinley GH, Basaran OA. 2010 Formation of beads-on-a-string structures during break-up of viscoelastic filaments. *Nat. Phys*. **6**, 625–631. (doi:10.1038/nphys1682)
27. Kröger R, Berg S, Delgado A, Rath HJ. 1992 Stretching behaviour of large polymeric and Newtonian liquid bridges in plateau simulation. *J. Non Newton. Fluid Mech*. **45**, 385–400. (doi:10.1016/0377-0257(92)80069-a)
28. Kröger R, Rath HJ. 1995 Velocity and elongation rate distributions in stretched polymeric and Newtonian liquid bridges. *J. Nonnewton. Fluid Mech*. **57**, 137–153. (doi:10.1016/0377-0257(94)01289-T)
29. Zhang X, Padgett RS, Basaran OA. 1996 Nonlinear deformation and breakup of stretching liquid bridges. *J. Fluid Mech*. **329**, 207–245. (doi:10.1017/S0022112096008907)
30. Tembely M, Vadillo D, Mackley MR, Soucemarianadin A. 2012 The matching of a 'one-dimensional' numerical simulation and experiment results for low viscosity Newtonian and non-Newtonian fluids during fast filament stretching and subsequent break-up. *J. Rheol.* **56**, 159–183. (doi:10.1122/1.3669647)
31. Vadillo DC, Tembely M, Morrison NF, Harlen OG, Mackley MR, Soucemarianadin A. 2012 The matching of polymer solution fast filament stretching, relaxation, and break up experimental results with 1D and 2D numerical viscoelastic simulation. *J. Rheol*. **56**, 1491–1516. (doi:10.1122/1.4749828)
32. Zhuang J, Ju YS. 2015 A combined experimental and numerical modeling study of the deformation and rupture of axisymmetric liquid bridges under coaxial stretching. *Langmuir* **31**, 10173–10182. (doi:10.1021/acs.langmuir.5b02102)
33. Scott S, Pfeffer M, Oppenheimer C, Bali E, Lamb OD, Barnie T, Woods AW, Kjartansdóttir R, Stefánsson A. 2023 Near-surface magma flow instability drives cyclic lava fountaining at Fagradalsfjall, Iceland. *Nat. Commun*. **14**, 6810. (doi:10.1038/s41467-023-42569-9)
34. Stovall WK, Houghton BF, Gonnermann H, Fagents SA, Swanson DA. 2011 Eruption dynamics of Hawaiian-style fountains: the case study of episode 1 of the Kīlauea Iki 1959 eruption. *Bull. Volcanol*. **73**, 511–529. (doi:10.1007/s00445-010-0426-z)
35. Pioli L, Harris AJL. 2019 Real-time geophysical monitoring of particle size distribution during volcanic explosions at stromboli volcano (Italy). *Front. Earth Sci*. **7**, 52. (doi:10.3389/feart.2019.00052)
36. Lesher CE, Spera FJ. 2015 Thermodynamic and transport properties of silicate melts and magma. In *The encyclopedia of volcanoes* (ed. H Sigurdsson), pp. 135–158. London: Elsevier. (doi:10.1016/B978-0-12-385938-9.00005-5)
37. Bagdassarov N, Dorfman A, Dingwell DB. 2000 Effect of alkalis, phosphorus, and water on the surface tension of haplogranite melt. *Am. Mineral*. **85**, 33–40. (doi:10.2138/am-2000-0105)
38. Gardner JE, Ketcham RA, Moore G. 2013 Surface tension of hydrous silicate melts: constraints on the impact of melt composition. *J. Volcanol. Geotherm. Res*. **267**, 68–74. (doi:10.1016/j.jvolgeores.2013.09.007)

39. Colucci S, Battaglia M, Trigila R. 2016 A thermodynamical model for the surface tension of silicate melts in contact with H2O gas. *Geochim. Et Cosmochim. Acta* **175**, 113–127. (doi:10.1016/j.gca.2015.10.037)
40. Mader HM, Llewellin EW, Mueller SP. 2013 The rheology of two-phase magmas: a review and analysis. *J. Volcanol. Geotherm. Res*. **257**, 135–158. (doi:10.1016/j.jvolgeores.2013.02.014)
41. Sork A *et al*. 2025 Size matters: a new view of the relationship between shape and size for molten volcanic ballistics. *Bull. Volcanol*. **87**, 61. (doi:10.1007/s00445-025-01845-w)
42. Jones TJ, Cashman KV, Liu EJ, Rust AC, Scheu B. 2022 Magma fragmentation: a perspective on emerging topics and future directions. *Bull. Volcanol*. **84**, 45. (doi:10.1007/s00445-022-01555-7)
43. Ogbuagu CC, Jones TJ. 2025 The in-flight deformation of pyroclasts: insights from analogue experiments. *Bull. Volcanol*. **87**, 33. (doi:10.1007/s00445-025-01814-3)
44. Gillies J. 2024 Textural evolution of pyroclasts in weakly explosive basaltic eruptions. Doctoral thesis, [Durham, UK]: Durham University. https://etheses.dur.ac.uk/15722/.
45. Taddeucci J, Alatorre-Ibargüengoitia MA, Cruz-Vázquez O, Del Bello E, Scarlato P, Ricci T. 2017 In-flight dynamics of volcanic ballistic projectiles. *Rev. Geophys*. **55**, 675–718. (doi:10.1002/2017rg000564)
46. Yildirim OE, Basaran OA. 2001 Deformation and breakup of stretching bridges of Newtonian and shear-thinning liquids: comparison of one- and two-dimensional models. *Chem. Eng. Sci*. **56**, 211–233. (doi:10.1016/s0009-2509(00)00408-5)
47. Allgood C, Jones TJ. 2025 Breakup dynamics of Newtonian fluids under extension [dataset] [Data set]. Zenodo. (doi:10.5281/zenodo.17341800)
48. Allgood C, Jones TJ. 2026 Supplementary material from: Breakup dynamics of Newtonian fluids under extension. Figshare. (doi:10.6084/m9.figshare.c.8285021)